Journal of Molecular Liquids 361 (2022) 119609

Contents lists available at ScienceDirect

Journal of Molecular Liquids

journal homepage: www.elsevier.com/locate/molliq

Insights into solvation effects, spectroscopic, Hirshfeld surface Analysis, reactivity analysis and anti-Covid-19 ability of doxylamine succinate: Experimental, DFT, MD and docking simulations

Jamelah S. Al-Otaibi [a,*], Y. Sheena Mary [b], Y. Shyma Mary [b], Nivedita Acharjee [c], S. Balachandar [d], H.S. Yathirajan [e]

[a] Department of Chemistry, College of Science, Princess Nourah Bint Abdulrahman University, P.O. Box 84428, Riyadh 11671, Saudi Arabia
[b] Thushara, Neethinagar-64, Pattathanam, Kollam, Kerala, India
[c] Department of Chemistry, Durgapur Government College, District-Paschim Bardhaman, West Bengal, India
[d] PG and Research Department of Chemistry, Vivekanandha College of Arts and Sciences for Women (Autonomous), Elayampalayam, Namakkal, Tamilnadu, India
[e] Department of Studies in Chemistry, University of Mysore, Manasagangotri, Mysore, Karanataka, India

ARTICLE INFO

Article history:
Received 16 March 2022
Revised 8 May 2022
Accepted 11 June 2022
Available online 15 June 2022

Keywords:
Doxylamine succinate: DFT
Docking
MD simulation
Wavefunction reactivity analysis

ABSTRACT

In the present work, the experimental and theoretical reports on electronic and vibrational features of doxylamine succinate (DXS) are presented. The vibrational spectra were documented and wavenumbers were obtained theoretically assigned by means of potential energy distribution. In DXS, N-H. . .O and C-H. . .O intermolecular hydrogen bonding contacts are associated with O. . .H/H. . .O interactions. Solvation free energy (SFE) for DXS in water, methanol and DMSO, are −10.67, −10.95 and −10.61 eV/mol respectively. Interpretation of electrostatic potential, electron localization function (ELF), localized orbital locator (LOL) as well as atoms-in-molecules (AIM) analysis is also performed. Presence of non-covalent interactions is evident from the non-covalent interaction (NCI) isosurface. Molecular docking and simulations were used to determine the binding energy of DXS in order to investigate its potential activity against the SARS-CoV-2 protease.

1. Introduction

Antihistaminic doxylamine succinate is often used to treat morning sickness in pregnant women. Because it is such a bitter medicine, it is critical to hide the bitter flavor [1]. Doxylamine succinate is a short-acting sedative made up of *N,N*-dimethyl-2[1-phenyl-1-(2-pyridinyl)ethoxy]-butanediote. It is sympathomimietic drug that's utilized as a nasal decongestant in cough and cold medicines [2]. Doxylamine is a short-acting sedative that can be used alone or in conjunction with other drugs to offer allergy and cold relief at night [3–6]. Doxylamine's pharmacokinetics and pharmaco-dynamics were studied in a phase I trial [7]. Recently researchers reported on the estimation of DXS in bulk and in pharmacological dosage form [8,9]. Parvez et al. reported XRD analysis of doxylamine succinate (DXS) [10]. Pyridine is an aromatic compound that has a variety of chemical and biological applications [11,12]. The pyridine ring structural motif is found in vitamin B3 and B6, as well as other nitrogenous plants. Thousands of drugs with biological functions contain the pyridine nucleus according to pharmaceutical data [13]. Pyridine and its derivatives are employed in the production of a variety of herbicides and pesticides, as well as a solvent in paints, and rubber products [14]. Arylated pyridines have a wide range applications including for a variety of medications, ligands for chemical synthesis and organic compounds in material science [15]. At different temperatures, Singh et al. investigated the volumetric behavior of glycine in aqueous succinic acid [16]. Succinic acid is a dicarboxylic acid that is widely employed in a variety of industries, including food, agriculture, pharmaceuticals and polymers. It works in conjunction with protein to rebuild nerve endings and aid in the fight against infection. Different amino acids are converted to succinic acid and had been demonstrated to be significant in feeding myocardial contractions with fuel under low oxygen conditions [17].

Using density functional theory (DFT), spectroscopic methods and docking to deduce the structural activity of a drug could open the path for the creation of novel antibacterial inhibitors. Despite the fact that DFT studies on pyridine derivatives have been

* Corresponding author.
E-mail addresses: jamelah2019@rediffmail.com, jsalotabi@pnu.edu.sa (J.S. Al-Otaibi).

https://doi.org/10.1016/j.molliq.2022.119609
0167-7322/

reported, no spectral study or DFT studies on doxylamine succinate (DXS) have been conducted [18–20].The use of quantum chemical computations supported by DFT in vibrational spectral analysis of DXS is an efficient way for analyzing the many forms of bonding and normal modes of vibration [21,22]. Potential energy distributions have been used to support the entire vibrational assignments for all vibrational modes. Natural bond orbital (NBO) and Hirshfeld analysis were used to do investigation of the intermolecular interactions and contacts. Docking against viral proteins was used to assess the antiviral efficacy of DXS. The structure of DXS has been investigated using theoretical and experimental calculations. FT-IR and FT-Raman spectra of DXS are explained experimentally and theoretically. The antiviral action was determined using molecular docking, which revealed that it may engage irreversible with the SARS-CoV-2 protease.

2. Methods

DXS, is obtained as a gift [10] and the vibrational spectra (Fig.S1 and Fig.S2) are recorded as in literature [23] and the calculations of DXS (Fig. 1) were by Gaussian 09 [24] and Gaussview 5 [25] via wB97XD/6–311++G* [26–28]. The default settings were used for the convergence criteria regarding self-consistent field and optimization procedure. The solvation free energies (SFEs) of DXS in different solvents were also estimated [29]. ELF and AIM topological studies and the calculations of NCI, LOL and electrostatic potential (ESP) plots were performed using Multiwfn software [30]. ELF, NCI and ESP *iso*-surfaces were visualized using UCSF Chimera and VMD software [31,32]. Molecular Docking studies are carried out for DXS with SARS-CoV-2 main protease (6YB7) with highest resolution 1.25 Å. The protein X-ray structure was downloaded from protein data bank [33] and subsequently cleaned for any steric clashes, intrinsic water and co-crystallized molecules. Then the protein structure was subjected to energy minimization using 1000 steps of conjugate gradient algorithm. All the hydrogen are properly added and saved in pdb for docking purpose. Docking studies were carried out in patch dock web server [34]. Grid center was provided as 0.35 Å × 6.0 Å × 3.0 Å. Docking parameters were set for protein small ligand with clustering root mean square deviation (RMSD) 0.5 Å. Ligand binding site information was uploaded in the server advanced parameter option and energy minimized protein and geometrically optimized DXS was uploaded for final run. The Desmond 2020.1 from Schrödinger, LLC was used to run molecular dynamics (MD) simulations on dock complexes for 6YB7 with DXS. Simple point charge (SPC) water molecules and the OPLS-2005 force field were utilized in this system [35] in a period boundary solvation box of 10 $Å^3$. Na^+ was supplied to system to neutralize the charge and NaCl solutions were added to replicate the physiological environment.

When retraining with the complexes with DXS, the system was first equilibrated using a normal volume and temperature (NVT) ensemble for 100 ns. After the preceding phase, a 12-ns normal pressure and temperature (NPT) ensemble run was used to perform a quick equilibration and reduction. Calculations were made to track the stability of MD simulations using parameters such as the RMSD, radius of gyration (Rg), root mean square fluctuation (RMSF0), H-bond number and solvent accessible surface area (SASA) [36].

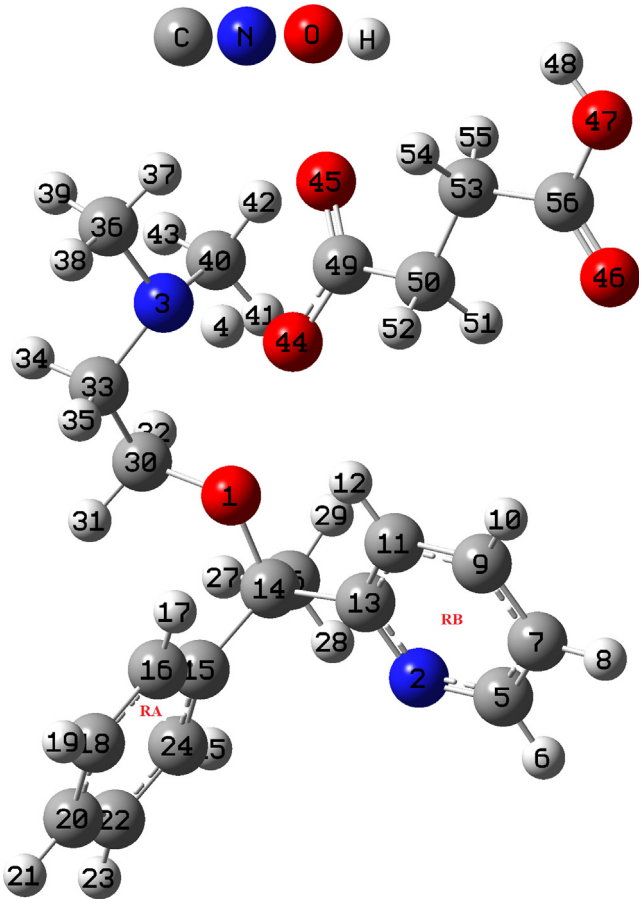

Fig. 1. Optimized geometry of DXS.

3. Results and discussion

3.1. Hirshfeld surface analyses

Hirshfeld surface analysis is a technique for validating the space taken by a molecule in a crystal system in order to divide the electron density into molecular pieces [37,38]. To define the near contacts in the crystal, the CrystalExplorer21 application was utilized [39], which can delineate the curvedness, shape index, electrostatic potential and fingerprint plots overlaid over d_{norm}. 2D fingerprint mapping and 3D Hirshfeld surfaces of DXS are depicted in Fig. 2. Intermolecular hydrogen bonding contact between N-H...O and C-H...O are related with O...H/H...O interactions, respectively which is appeared as a sharp edge and a lengthy symmetric spikes upon 2D mapping with a percentage contribution of 24.5. The most remarkable inter/intra atomic contact is H...H (center of 2D map) which contributes about 55.7% and it is due to three methyl groups (C-H...H-C) available in DXS. On the other hand, 15% contribution of centroid/centroid contacts to the total Hirshfeld surface is supposed as a pair of wings in 2D fingerprint mapping. Weak pi...pi contact is evaluated as 1% that evidenced the lack of π...π intermolecular interactions in the crystal system [40,41]. The suppressive contacts of π...π is due to the excessive intermolecular H...H (C-H...H-C) and O...H (N-H...O/C-H...O) interactions. Because of its positive charge, the nitrogen ion in ammonium moiety does not participate in intermolecular N...H interactions, and the minor participation of N...H (3.7%) is attributed to nitrogen (pyridine moiety) interacting with adjacent hydrogen's.

A strong red spot is appeared on the O-H group of acidic moiety in d_{norm} which intensely explained the DXS has strong interaction sites. In connection, a countable number of faint red spots where also been noticed on both the acidic and basic parts evidenced the weaker C-H...O/C-H...N interactions. With the inverted blue and red coloured bow-tie pattern, the shape index confirms the presence of weaker π...π interaction in the system and as flat regions on the curvedness [42].

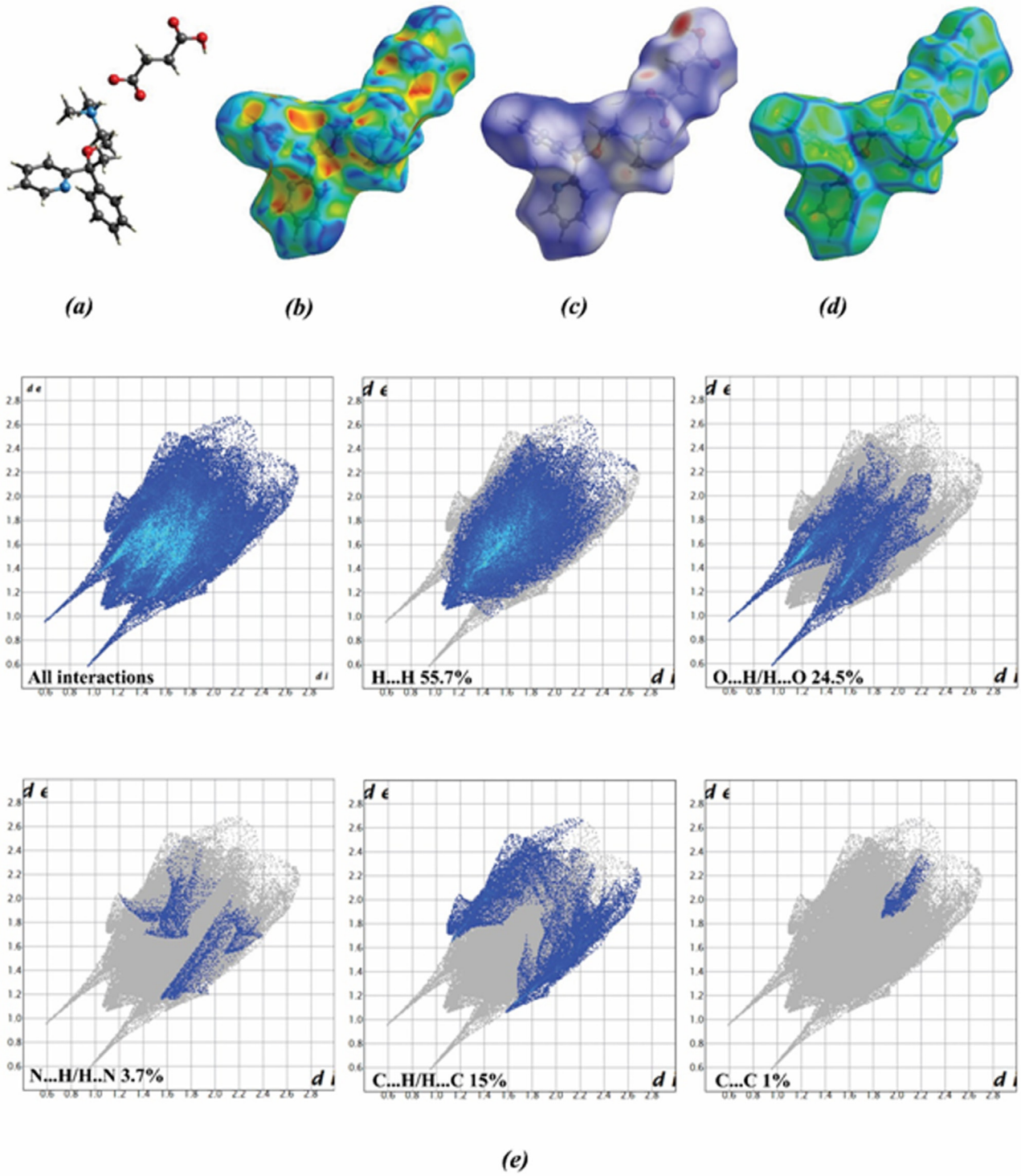

Fig. 2. Hirshfeld surface plots of S6 mapped with three-dimensional (a) open view, (b) shape index, (c) dnorm, (d) curvedness and its (e) two dimensional fingerprint contacts with its percentage contribution.

3.2. Spectroscopic geometric and electronic properties

Ring vibrations (table S1) are at: 3063, 3033 cm^{-1} (Raman), 3078–3033 cm^{-1} (DFT) (υCH); 1575, 1560, 1433 cm^{-1} (IR), 1572, 1483, 988 cm^{-1} (Raman), 1575–986 cm^{-1} (DFT) (υRA); 1325 cm^{-1} (IR), 1321, 1181 cm^{-1} (Raman), 1327–1014 cm^{-1} (DFT) (δCH) and 992, 692 cm^{-1} (IR), 850 cm^{-1} (Raman), 990–697 cm^{-1} (DFT (γCH) for the mono substituted phenyl ring RA and 3075, 3052 cm^{-1} (IR), 3075–3040 cm^{-1} (DFT) (υCH), 1553, 1539, 1419, 1024 cm^{-1} (IR), 1281, 1022 cm^{-1} (Raman), 1554–1023 cm^{-1} (DFT) (υRB), 1250–1042 cm^{-1} (DFT) (δCH) and 935, 761 cm^{-1} (IR), 931 cm^{-1} (Raman), 973–761 cm^{-1} (DFT) (γCH) for the pyridine ring RB [43–45]. The pyridine ring stretching modes are reported at 1603, 1536, 1496, 1260 cm^{-1} (IR), 1594,

1263 cm^{-1} (Raman) and 1590–1265 cm^{-1} (DFT) and the bending modes in the region, 1334–1063 cm^{-1} and 949–793 cm^{-1} theoretically [46].

The CH_3 modes are assigned theoretically in the ranges: 3034–2910 cm^{-1} (υCH_3), 1502–966 cm^{-1} (δCH_3) while bands are observed at 3034, 3018, 2984 cm^{-1} (IR), 2996, 2981, 2918 cm^{-1} (Raman) for stretching and 1504, 1470, 1406, 1140, 1093, 1072 cm^{-1} (IR), 1406, 1376, 1152 cm^{-1} (Raman) for bending modes [43,47]. The CH_2 modes are assigned at: 2963, 2932, 2882 cm^{-1} (IR), 2967, 2932, 2880 cm^{-1} (Raman), 2975–2883 cm^{-1} (DFT) as stretching and 1490, 1445, 1381, 1260, 1238, 919 cm^{-1} (IR), 1450, 1272, 1238 cm^{-1} (Raman), 1492–918 cm^{-1} (DFT) as bending modes [43].

The υC = O and υCO are assigned at 1675, 1600, 1535 cm^{-1} and at 1219, 1113, 1097, 1053, 1006 cm^{-1} theoretically while modes are observed at 1680, 1610, 1533, 1220, 1093 cm^{-1} (IR) and 1672, 1601, 1533, 1221, 1103, 1051, 1004 cm^{-1} (Raman) experimentally [43,48] and the corresponding reported values are at 1677, 1611 and 1101 cm^{-1} [48,49]. The N. . .H. . .O and OH modes are assigned at 1720 and 3511 cm^{-1} theoretically [50] while CN stretches are at 970, 896 and 833 cm^{-1} theoretically.

The CO bond lengths are 1.2237, 1.2702, 1.3137, 1.3997, 1.4466 and 1.4869 Å [10]. The separation, N3. . .H4. . .O44 = 2.5453 and the lengths N3-O45, N3-O44 and N3-O1 lengths are 3.2198, 2.5453 and 2.9107 Å gives significant hydrogen bonding [10]. The torsion angle between pyridine and phenyl ring is 71.9° and other important torsion angles are: O1-C30-C33-N3, C30-C33-N3-C36, C13-C14-O1-C30, and C14-O1-C30-C33 angles are 55.8, 45.2, 172.5, and 162.1° [10].

Frontier molecular orbital (FMO) is used to characterize electron donating/withdrawing ability of any chemical system by predicting the chemical reactivity and kinetic stability of molecules [51,52]. A smaller HOMO-LUMO gap gives the molecule's stabilization [53,54]. For DXS, HOMO is located on the nitrogen and oxygen atoms of aliphatic moieties and a lesser extent on the aromatic ring system (Fig. 3). On the other hand, LUMO electrons were spread over on the aromatic ring system in a greater extent and resonate well. The calculated energy gap of HOMO-LUMO was 5.7505 eV, which gives a possible charge transfer in DXS [55]. SFE is the change in energy of a molecule between gas and solvent, and it is useful in predicting parameters such as activity coefficients and solubilities [56]. Continuum solvation models are employed in this context to predict SFEs [29,57]. SFEs for DXS were computed using SMD model in water, methanol and DMSO, yielding values of −10.67, −10.95 and −10.61 eV/mol respectively. SFE are negative for all solvents which are nearly same and all solvents are better for solubilization of DXS which supports the biological activity. The chemical descriptors in solvents show slight variations in comparison with that in vacuum. The changes in thermochemical parameters are negative for all solvents,which means the solvation process is exothermic and spontaneous.

ESP exhibits reactive sites of electrophilic or nucleophilic attacks [58,59]. The negative and positive ESP sites are shown as red and blue in the ESP surfaces. Fig. 4 depicts the electrostatic potential of DXS. It exhibits a positive potential on H3 of acidic COOH and N2 with (CH_3-N-CH_3) dimethyl system [60]. These positive atoms can naturally interact with negative system of the opponent. Similarly, Oxygen atoms reveal a strong electron rich centre around it and it would interact with positive system [61]. Strong NBO interactions due to lone pair atoms are: N2→ (C5-C7, C11-C13) with energies, 9.01 and 9.57 and O44→ (O45-C49) with energy 77.39, O45→ (O44-C49, C59-C50) with energy (20.30, 17.24) and O46→ (O47-C56, C53-C56) with energy (35.09, 17.20) and O47→ (O46-C56) with energy 40.45 kcal/mol (table S2) [62]. Occupancy is 100% p-character in O44, O45 and O46 atoms [63].

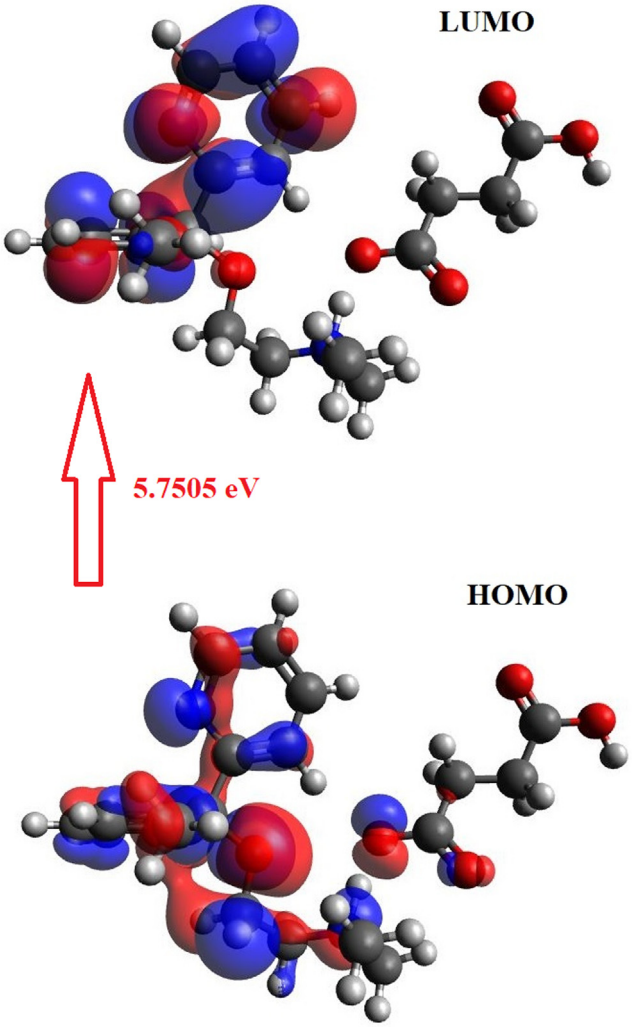

Fig. 3. HOMO-LUMO plots of DXS.

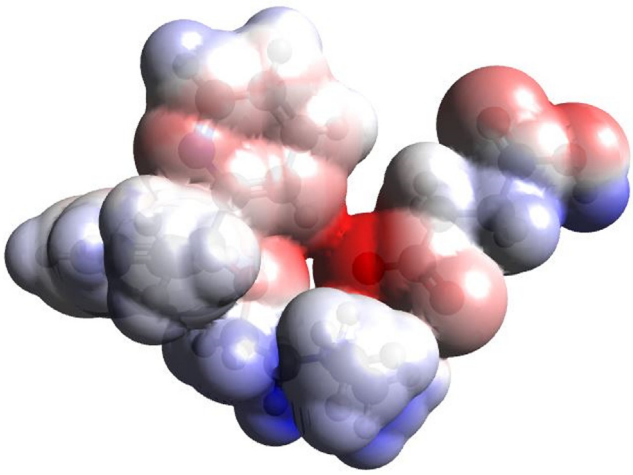

Fig. 4. ESP plot of DXS.

3.3. Reactivity analysis

Analysis of ELF [64,65] was performed to obtain electronic structure with the ELF localizarion domain of DXS (Fig.S3)

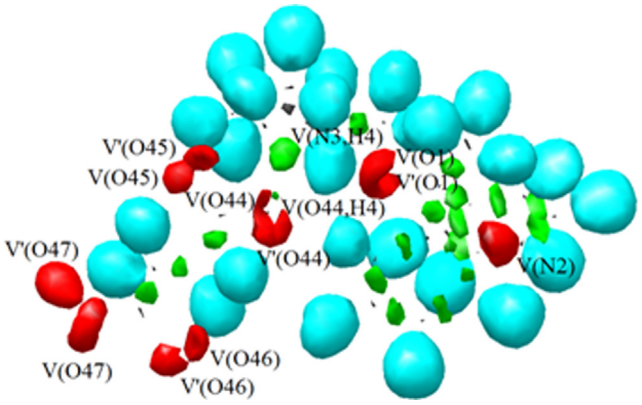

Fig. 5. ELF localization domains (Isovalue = 0.80) of DXS. The protonated basins are shown in blue, monosynaptic basins are marked in red, disynaptic basins are marked in green and the core basins are marked in red color. (For interpretation of the references to color in this figure legend, the reader is referred to the web version of this article.)

displayed in Fig. 5. The presence of monosynaptic V(O44) basin integrating 3.88 e is with the non-bonding electron density (NBED) at O44 carbon, while the disynaptic V(O44,H4) basin integrating 2.30 e is associated with the O44-H4 bonding region. Monosynaptic V(O45) and V'(O45) with 5.94 e is related to NBED at O45 oxygen. The ELF also gives V(O1) and V'(O1) basins integrating 5.57 e, monosynaptic V(O46) and V'(O46) basins integrating 5.58 e, monosynaptic V(O47) and V'(O47) basins with 5.07 e, associated respectively with NBED on O1, O46 and O47. Decrease in NBED at O47 is attributed to formation of O-H bond. The monosynaptic V(N2) and V(N3) with 3.02 and 0.35 e is related to the NBED at N2 and N3, while disynaptic V(N3,H4) basin with 2.22 e is with N3-H4 region. Note that monosynaptic V(N3) basin shows minimal population of 0.35 e, owing to the involvement of the electron density at N3 nitrgogen in the N3-H4 bonding region [66].

Analysis of the QTAIM parameters [67,68] allows obtaining a complete comprehension of the atomic interactions present in a molecule. The total electron density (ED), ρ, Laplacian of electron density (LED) $\nabla^2\rho(r_c)$ and the localized orbital locator (LOL) in a.

Table 1
Total electron density, ρ, Laplacian of electron density $\nabla^2\rho(r_c)$ and localized orbital locator (LOL) in au at the selected BCP (3,-1) and RCP (3, +1) of DXS (Numbering according to the optimized geometry in Fig. 5)

BCP (3,-1)					**RCP** (3,+1)				
CP	Bonding Region	ρ	$\nabla^2\rho(r_c)$	LOL	CP	Ring/Bonding Region	ρ	$\nabla^2\rho(r_c)$	LOL
61	N2-C5	0.302	−0.630	0.680	63	Pyridine Ring	0.023	0.151	0.142
65	N2-C13	0.302	−0.636	0.692	75	Phenyl ring	0.022	0.136	0.138
73	C56-O46	0.379	−0.562	0.591	78	C49, O44, H12, C11,C9, C10, H52, C50	0.001	0.006	0.029
84	C56-O47	0.247	−0.333	0.647	98	O44,H4,O1,C14, C13, C11	0.294	0.024	0.041
90	O46-H12	0.014	0.071	0.135	108	O44,C49,O45, H37, N3, H4	0.007	0.044	0.073
100	C49-O44	0.306	−0.555	0.663	109	O44,C49,O45, H37, N3, H4	0.006	0.038	0.067
101	C30-O1	0.218	−0.221	0.625					
102	C49-O45	0.342	−0.651	0.645					
103	O44-H4	0.099	0.114	0.472					
112	O45-H42	0.008	0.043	0.010					
113	O45-H37	0.013	0.064	0.130					

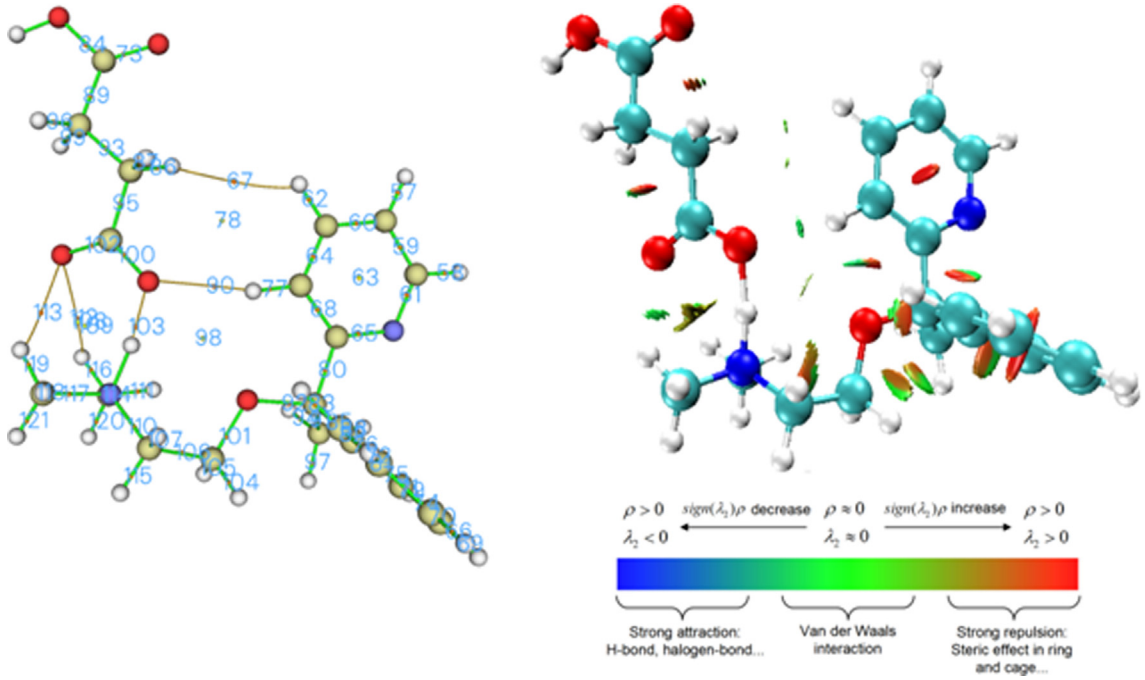

Fig. 6. BCPs (3,-1), RCPs (3,+1) and the bond paths along with the NCI isosurface of DXS.

u. selected BCP (3,-1) and RCP (3, +1) of DXS are given in Table 1, with the BCPs and RCPs displayed in Fig. 6 along with the NCI [69] *iso*-surface. BCP 61 and 65 are associated with the N2-C5 and N2-C13 of the pyridine ring and show electron density of 0.302 e, with the LOL of 0.680 and 0.692 au, with the negative Laplacian of −0.630 and −0.636 au. The C56-O46 double bond shows the total electron density of 0.379 e and that of C56-O47 single bond is 0.247 e, with the respective LOL of 0.591 and 0.647 au. BCP 90, 112 and 113 associated with the O46-H12, O45-H42 and O45-H37 bonds show the total electron density of 0.014, 0.008 and 0.013 e and LOL of 0.135, 0.010 and 0.130 respectively, while BCP 103 associated with the O44-H4 bonding region shows the higher accumulation of total electron density of 0.099 e and LOL of 0.472, with the positive LED characteristic of non-covalent interactions. DXS shows six ring critical points (RCPs), two of them, namely RCP 63 and 75 are associated with the pyridine and phenyl rings with the ED of 0.023 and 0.022 e and LOL of 0.142 and 0.138 au. RCPs 78, 98, 108 and 109 are associated with the atomic framework created due to non-covalent interactions in the molecule. Note that RCP 98 shows the maximum total electron density of 0.294 e and is associated with the bonding framework of O44, H4, O1, C14, C13 and C11 with the positive Laplacian of 0.024 au, implying the presence of non-covalent interactions, evident from the NCI isosurface shown in Fig. 6 [70].

The molecular electrostatic potential (MEP) study was performed to characterize the electrophilic and the nucleophilic sites of DXS and the MEP surface map is displayed in Fig. 7. The red and blue regions indicate positive and negative zones respectively. DXS shows the presence of 10 surface minima (blue color) and 19 surface maxima (brown color) in the MEP plot. The surface minima of −49.71 and −34.14 kcal mol^{-1} is localized near O44 and H4, while the surface maxima of + 27.38 and + 27.87 kcal mol^{-1} are localized over N3 nitrogen, implying the polarization of electronic charge along O44-H4-N3 framework. Note that the maximal MEP (+60.26 kcal mol^{-1}) is shown by the surface maxima at the vicinity of H48, while the surface minima of −53.88 and −58.88 kcal mol^{-1} are localized around O46 and O47.

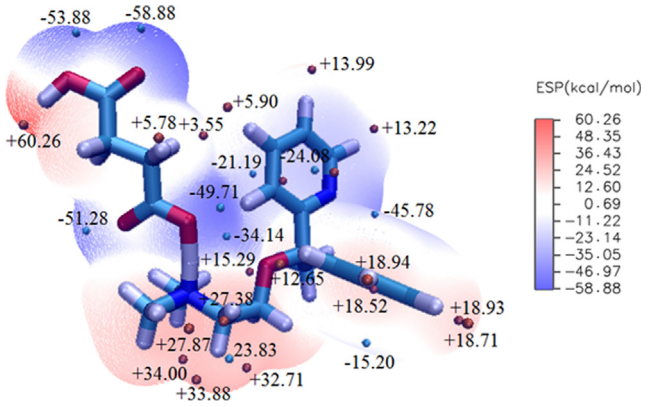

Fig. 7. Molecular Electrostatic Potential (MEP) isosurface with the electrostatic potential (ESP) in kcal mol^{-1} of the surface minima (blue colour) and surface maxima (brown color). (For interpretation of the references to color in this figure legend, the reader is referred to the web version of this article.)

3.4. Molecular Docking and dynamics simulations

Docking of DXS with SARS-CoV-2 main protease (PDB ID: 6YB7) are displayed in Fig.S4. Surface view and ribbon secondary structure of DXS with SARS-CoV-2 main protease displayed that the

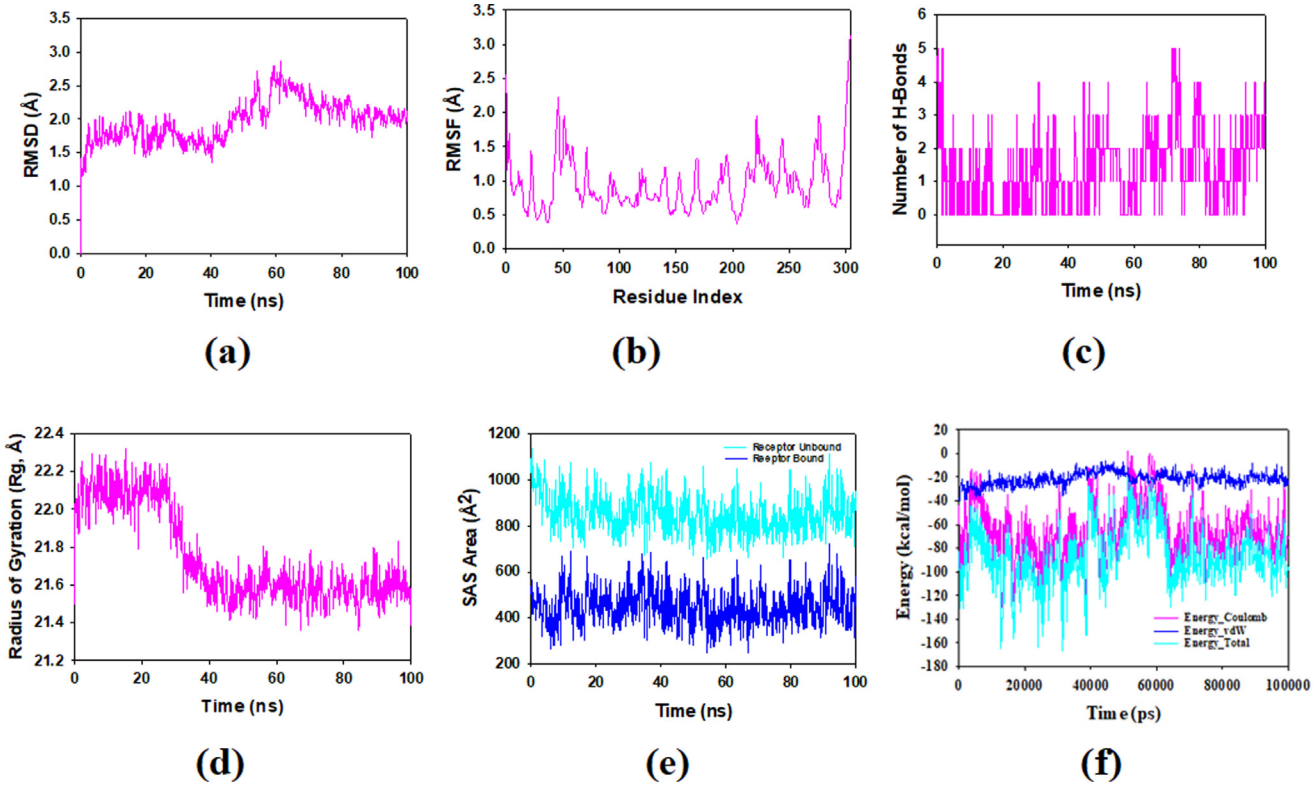

Fig. 8. MD simulation analysis of 100 ns trajectories of (a) Cα backbone of SARS-CoV-2 main protease + DXS (b) RMSF of Cα backbone of SARS-CoV-2 main protease + DXS (c) Formation of hydrogen bonds in SARS-CoV-2 main protease + DXS complex. (d) Radius of gyration (Rg) of Cα backbone of SARS-CoV-2 main protease + DXS (e) Solvent accessible surface area of SARS-CoV-2 main protease + DXS complex (f) Energy plot of SARS-CoV-2 main protease + DXS complex.

co-crystal well accommodated within in the binding pocket (Fig. S4b). The dock score is calculated within 0.5 Å RMSD clusters tolerance 6180 with an area 710.15. The free energy of binding of DXS exhibited more negative (ΔG) = -8.7 kcal/mol. This indicated the high binding affinity of DXS for SARS-CoV-2 main protease. Residues Asn142, Ser144 and His163 formed conventional hydrogen bonds (2.6875 and 2.9230 Å) with the DXS (Fig.S4), whereas, the other residues at the binding pocket involved in weak interactions with the DXS.

MD studies of 100 ns give stability and convergence of CoV-main protease (PDB ID: 6YB7) with DXS. RMSD of Cα-backbone of complex exhibited a deviation of 0.6 Å (Fig. 8(a)). Plot of stable RMSD during simulation signify a good convergence and stable conformations [71]. Therefore, it can be suggested that DXS bound to SARS-CoV-2 main protease as a quite stable complex due to higher affinity of the ligand. The RMSF plots displayed small spikes of fluctuation in SARS-CoV-2 main protease protein except at residues 48–60, 220–240 and 260–280 residues might be due to higher flexibility of the residues conformed into loop region, while the rest of the residues less fluctuating during 100 ns simulation on binding with DXS (Fig. 8(b)) indicating the stable amino acid conformations during the simulation time. All these RMSF values are in the acceptable region [72] and during simulation structures of proteins are stable in ligand bound conformations. Number of H-bonds between protein and ligand suggests significant interaction and stability of the complex. The H-bonds number showed significant numbers between DXS bound with SARS-CoV-2 main protease, respectively throughout the simulation time 100 ns (Fig. 8 (c)). A consistent numbers of hydrogen bonds are observed between protein and DXS (Average 2 number) (Fig. 8(c)) that might facilitate to conform into stable complex. Rg gives protein's compactness and in this study, SARS-CoV-2 main protease Cα-backbone bound to DXS displayed lowering of Rg from 22.0 to 21.5 Å (Fig. 8(d)). Significantly lowering gyration (Rg) indicates highly compact orientation of the protein in ligand bound state [73,74]. The unbound state of DXS to receptor protein SARS-CoV-2 main protease show high SASA (Fig. 8(e), Cyan) and lowered during bound state with DXS (Fig. 8(e), blue). The overall study of Rg signifies ligand binding compel the proteins to become more compact and less flexible. Energy plots describe the total energy of the protein ligand complex in Fig. 8(f). More negative values indicate more compact and stable structure. It is observed from Fig. 8(f), SARS-CoV-2 main protease bound with DXS achieved global minima with an average energy −105 kcal/mol. In order to achieve the global minima, major contribution is provided by coulomb energy and nonetheless by van der Waal's (vdW) energy (Fig. 8((f)). Energy plots indicated that DXS accommodated in the binding cavity of the protein and facilitate in stabilizing protein as well as to make a compact complex [75].

4. Conclusion

Vibrational spectroscopic, electronic properties and reactivity analysis of doxylamine succinate were reported theoretically and experimentally. The most remarkable inter/intra atomic contact is H. . .H and it is due to three methyl groups. The MEP maps provide information about the reactivity sites of DXS. Maximum total electron density is associated with the bonding framework of O44, H4, O1, C14, C13 and C11 with a positive Laplacian, implying the presence of non-covalent interactions. The dock score is within 0.5 Å RMSD clusters tolerance is 6180 and binding free energy is more negative. According to docking and MD simulations DXS interacted favorably with SARS-CoV-2 main protease with energy of −105 kcal/mol.

CRediT authorship contribution statement

Jamelah S. Al-Otaibi: Conceptualization, Methodology, Data curation, Software, Validation. **Y. Sheena Mary:** Conceptualization, Methodology, Data curation, Software, Validation. **Y. Shyma Mary:** Conceptualization, Methodology, Data curation, Software, Validation. **Nivedita Acharjee:** Conceptualization, Methodology, Data curation, Software, Validation. **S. Balachandar:** Conceptualization, Methodology, Data curation, Software, Validation. **H.S. Yathirajan:** Conceptualization, Methodology, Data curation, Software, Validation.

Declaration of Competing Interest

The authors declare that they have no known competing financial interests or personal relationships that could have appeared to influence the work reported in this paper.

Acknowledgments

The authors express their gratitude to Princess Nourah Bint Abdulrahman University Researchers Supporting Project number (PNURSP2022R13), Princess Nourah bint Abdulrahman University, Riyadh, Saudi Arabia

Appendix A. Supplementary material

Supplementary data to this article can be found online at https://doi.org/10.1016/j.molliq.2022.119609.

References

[1] T.Y. Puttewar, M.D. Kshirsagar, A.V. Chandewar, R.V. Chikhale, Formulation and evaluation of orodispersible tablet of taste masked doxylamine succinate using ion exchange resin, Journal of King Saud University (Science) 22 (2010) 229–240, https://doi.org/10.1016/j.jksus.2010.05.003.
[2] R. Eccles, I. Fietze, U.B. Rose, Rationale for treatment of common cold and flu with multi-ingredient combination products for multi-symptom relief in adults, Journal of Respiratory diseases 4 (2014) 73–82, https://doi.org/10.4236/ojrd.2014.43011.
[3] S.V. Rajani, I. SowkarBaig, R.N.P. Amulya, A validated simultaneous estimation of doxylamine succinate and pyridoxine hydrochloride by UV-spectrophotometric method in bulk and formulation, Int. J. Pharm. Res. Anal. 4 (2014) 139–143, https://doi.org/10.29088/SAMI/AJCA.2019.2.245255.
[4] R. Gadsby, A.M. Barnie-Adshead, Prospective study of nausea and vomiting during pregnancy, Br. J. Gen. Pr 43 (1993) 245–248, PMCID: PMC1372422.
[5] N.M. Lee, S. Saha, Nausea and vomiting of pregnancy, Gastroenterol Clin. North Am. 40 (2011) 309–334, https://doi.org/10.1016/j.gtc.2011.03.009.
[6] E. Pope, C. Maltepe, G. Koren, Comparing pyridoxine and doxylamine succinate-pyridoxine HCl for nausea and vomiting of pregnancy: a matched, controlled cohort study, J. Clin. Pharmacol. 55 (2015) 809–814, https://doi.org/10.1002/jcph.480.
[7] M. Allison, C. Hale, A phase I study of the pharmacokinetics and pharmaco dynamics of intranasal doxylamine in subjects with chronic intermittent sleep impairment, Drugs 18 (2018) 129–136, 101.007/s40268-018-0232-1.
[8] S. Premkumar, A. Karunakaran, V. Murugesan, J. Munusamy, R. Jayaprakash, R. Murugesan, Validated UV-spectrophotometric method for the simultaneous estimation of pyridoxine hydrochloride and doxylamine succinate in bulk and in pharmaceutical dosage form, Advanced Journal of Chemistry, A 2 (2019) 245–255, https://doi.org/10.33945/SAMI/AJCA.2019.2.245255.
[9] B.P. Kumar, S. Vidyadhara, T.E.G.K. Murthy, R.L.C. Sasidhar, V.S. Krishna, Development and validation of RP-HPLC method for simultaneous estimation of doxylamine succinate and pyridoxine hydrochloride in bulk and pharmaceutical dosage forms, Eurasian J. Anal. Chem. 12 (2017) 459–468, https://doi.org/10.12983/ejac.2017.00182a.
[10] M. Parvez, S. Dalrymple, A. Cote, Doxylamine hydrogen succinate, Acta Cryst. E 57 (2001) o163–o165, https://doi.org/10.1107/S160053680100085X.
[11] S.D. Banik, A. Chandra, A hybrid QM/MM simulation study of intramolecular proton transfer in the pyridoxal 5'-phosphate in the active site of transaminase: influence of active site interaction on proton transfer, J. Phys. Chem. B 118 (2014) 11077–11089, https://doi.org/10.1021/jp506196m.
[12] M. Mure, C.R. Kurtis, D.E. Brown, M.S. Rogers, W.S. Tambyrajah, C. Saysell, C.M. Wilmot, S.E. Phillips, P.F. Knowles, D.M. Dooley, M. McPherson, Activesite rearrangement of the 2-hydrazinopyridine adduct in Escherichia coli amine

oxidase to an azo copper(II) chelate form: a key role for tyrosine 369 in controlling the mobility of the TPQ-2HP adduct, Biochemistry 44 (2005) 1583–1594, https://doi.org/10.1021/bi0479860.
[13] S. Prachayasittikul, R. Pingaew, A. Worachartcheewan, N. Sinthupoom, V. Prachayasittikul, S. Ruchirawat, V. Prachayasittikul, Roles of pyridine and pyrimidine derivatives as privileged scaffolds in anticancer agents, Mini Rev. Med. Chem. 17 (2017) 869–901, https://doi.org/10.2174/1389557516666160923125801.
[14] D.H. Lataye, I.M. Mishra, I.D. Mall, Removal of pyridine from aqueous solution by adsorption on bagasse fly ash, Ind. Eng. Chem. Res. 45 (2006) 3934–3943, https://doi.org/10.1021/ie051315w.
[15] M. Akram, M. Adeel, M. Khalid, M.N. Tahir, H. Asghar, R. Aliabad, M.A. Ullah, J. Iqbal, A.A.C. Braga, Highly efficient one pot palladium-catalyzed synthesis of 3,5-bis(arylated)pyridines: comparative experimental and DFT studies, J. Mol. Struct. 1213 (2020), https://doi.org/10.1016/j.molstruc.2020.128131 128131.
[16] G. Singh, P. Patyar, T. Kaur, G. Kaur, Volumetric behavior of glycine in aqueous succinic acid and sodium succinate buffer at different temperatures, J. Mol. Liquid. 222 (2016) 804–817, https://doi.org/10.1016/j.molliq.2016.07.042.
[17] B. Bai, J.-M. Zhou, M.-H. Yang, Y.-L. Liu, X.-H. Xu, L.-M. Xing, Efficient production of succinic acid from macroalgae hydrolysate by metabolically engineered Escherichia coli, Bioresource Technology 185 (2015) 56–61, https://doi.org/10.1016/j.biortech.2015.02.081.
[18] R. Ullah, H. Ullah, A.A. Shah, S. Bilal, K. Ali, Oligomeric synthesis and density functional theory of leucoemeraldine base form of polyaniline, J. Mol. Struct. 1127 (2017) 734–741, https://doi.org/10.1016/j.molstruc.2016.08.009.
[19] A.R.B. Mohd Yusoff, A. Mahata, M. Vasilopoulou, H. Ullah, B. Hu, W. Jose da Silva, F. Kurt Schneider, P. Gao, A.V. Ievlev, Y. Liu, O.S. Ovchinnikova, F. De Angelis, M. Khaja Nazeeruddin, Observation of large rashba spin-orbit coupling at room temperature in compositionally engineered perovskite single crystals and application in high performance photodetectors, Materialstoday 46 (2021) 18–27.
[20] M. Sookhakian, H. Ullah, M.A.M. Teridi, G.B. Tong, W.J. Basirun, Y. Alias, Boron-doped graphene-supported manganese oxide nanotubes as an efficient non-metal catalyst for the oxygen reduction, Sustainable, Energy Fuels 4 (2020) 737–749, https://doi.org/10.1039/C9SE00775J.
[21] O. Ola, H. Ullah, Y. Chen, K. Thummavichai, N. Wang, Y. Zhu, DFT and experimental studies of iron oxide-based nanocomposites for efficient electrocatalysis, J. Mater. Chem. C 9 (2021) 6409–6417, https://doi.org/10.1039/D1TC01022K.
[22] H. Ullah, A. Loh, D.P. Trudgeon, X. Li, Density functional theory study of NiFeCo trinary oxy-hydroxides for an efficient and stable oxygen evolution reaction catalyst, ACS Omega 5 (2020) 20517–20524, https://doi.org/10.1021/acsomega.0c02679.
[23] A.S. El-Azab, Y.S. Mary, C.Y. Panicker, A.A.M. Abdel-Aziz, I.A. Al-Suwaidan, C. Van Alsenoy, FT-IR, FT-Raman and molecular docking study of ethyl 4-(2-(4-oxo-3-phenethyl-3,4-dihydroquinazolin-2-ylthio)acetamido)benzoate, J. Mol. Struct. 1111 (2016) 9–18, https://doi.org/10.1016/j.molstruc.2016.01.041.
[24] Gaussian 09, Revision B.01, M.J. Frisch, G.W. Trucks, H.B. Schlegel, G.E. Scuseria, M. A. Robb, J.R. Cheeseman, G. Scalmani, V. Barone, B. Mennucci, G.A. Petersson, H. Nakatsuji, M. Caricato, X. Li, H.P. Hratchian, A.F. Izmaylov, J. Bloino, G. Zheng, J.L. Sonnenberg, M. Hada, M. Ehara, K. Toyota, R. Fukuda, J. Hasegawa, M. Ishida, T. Nakajima, Y. Honda, O. Kitao, H. Nakai, T. Vreven, J.A. Montgomery, Jr., J.E. Peralta, F. Ogliaro, M. Bearpark, J.J. Heyd, E. Brothers, K.N. Kudin, V.N. Staroverov, T. Keith, R. Kobayashi, J. Normand, K. Raghavachari, A. Rendell, J.C. Burant, S.S. Iyengar, J. Tomasi, M. Cossi, N. Rega, J.M. Millam, M. Klene, J.E. Knox, J.B. Cross, V. Bakken, C. Adamo, J. Jaramillo, R. Gomperts, R.E. Stratmann, O. Yazyev, A.J. Austin, R. Cammi, C. Pomelli, J.W. Ochterski, R.L. Martin, K. Morokuma, V.G. Zakrzewski, G.A. Voth, P. Salvador, J.J. Dannenberg, S. Dapprich, A.D. Daniels, O. Farkas, J.B. Foresman, J.V. Ortiz, J. Cioslowski, D.J. Fox, Gaussian, Inc., Wallingford CT, 2010.
[25] R. Dennington, T. Keith, J. Millam, Gaussview, Version 5, Semichem Inc., Shawnee Mission, KS, 2009.
[26] A.D. Becke, Density-functional exchange-energy approximation with correct asymptotic behavior, Phys. Rev. A 38 (1988) 3098–3100, https://doi.org/10.1103/PhysRevA.38.3098.
[27] C. Lee, W. Yang, R.G. Parr, Development of the Colle-Salvetti correlation-energy formula into a functional of the electron density, Phys. Rev. B 37 (1988) 785–789, https://doi.org/10.1103/PhysRevB.37.785.
[28] J.-D. Chai, M. Head-Gordon, Long-range corrected hybrid density functionals with damped atom-atom dispersion corrections, Phys. Chem. Chem. Phys. 10 (2008) 6615–6620, https://doi.org/10.1039/B810189B.
[29] A.V. Marenich, C.J. Cramer, D.G. Truhlar, Universal solvation model based on solute electron density and on a continuum model of the solvent defined by the bulk dielectric constant and atomic surface tensions, J. Phys. Chem. B 113 (2009) 6378–6396, https://doi.org/10.1021/jp810292n.
[30] T. Lu, F. Chen, Multiwfn: A multifunctional wavefunction analyzer, J. Comp. Chem. 33 (2012) 580–592, https://doi.org/10.1002/jcc.22885.
[31] W. Humphrey, A. Dalke, K. Schulten, VMD: visual Molecular Dynamics, J. Mol. Graphics 14 (1) (1996) 33–38.
[32] E.F. Pattersen, T.D. Goddard, C.C. Huang, G.S. Couch, D.M. Greenblatt, C.C. Meng, T.E. Ferrin, UCSF Chimera—a visulaizaiton system for exploratory research and analysis, J. Comput. Chem. 25 (2004) 1605–1612, https://doi.org/10.1002/jcc.20084.
[33] https://www.rcsb.org/structure/6yb7
[34] https://bioinfo3d.cs.tau.ac.il/PatchDock/php.php
[35] W.L. Jorgensen, J. Chandrasekhar, J.D. Madura, R.W. Impey, M.L. Klien, Comparison of simple potential functions for simulating liquid water, J. Chem. Phys. 79 (1983) 926–935, https://doi.org/10.1063/1.445869.
[36] G.J. Martyna, D.J. Tobias, M.L. Klein, Constant pressure molecular dynamics algorithms, J. Chem. Phys. 101 (1994) 4177–4189, https://doi.org/10.1063/1.467468.
[37] J.J. McKinnon, M.A. Spackman, A.S. Mitchell, Novel tools for visualizing and exploring intermolecular interactions in molecular crystals, Acta Cryst. B 60 (2004) 627–668, https://doi.org/10.1107/s010876810402300.
[38] M.A. Spackman, D. Jayatilaka, Hirshfeld surface analysis, CrystEngComm. 11 (2009) 19–32, https://doi.org/10.1039/B818330A.
[39] S.K.Wolff, D.J.Grimwood, J.J.McKinnon, M.J.Turner, D.Jayatilaka, M.A. Spackman, CrystalExplorer -ver. 3.1, (University of Western Australia), 2012.
[40] A.D. Martin, J. Britton, T.L. Easun, A.J. Blake, W. Lewis, M. Schroder, Hirshfeld surface investigation of structure-directing interactions with dipicolinic acid derivatives, Cryst. Growth Des. 15 (2015) 1697–1706, https://doi.org/10.1021/cg5016934.
[41] J.B. Nanubolu, K. Ravikumar, Designing a new cocrystal of olanzapine drug and observation of concomitant polymorphism in a ternary cocrystal systems, CrystEngComm. 19 (2017) 355–366, https://doi.org/10.1039/C6CE02227H.
[42] S. Balachandar, M. Sethuram, P. Muthuraja, M. Dhandapani, Bioactivity of a radical scavenger bis(pyrazolium p-toluenesulphonate) on ctDNA and certain microbes: a combined experimental and theoretical analysis, Toxicol Res. 8 (2019) 421–431, https://doi.org/10.1039/C8TX00258D.
[43] N.P.G. Roeges, A guide to the complete interpretation of infrared spectra of organic structures, New York, John Wiley and Sons Inc., NY, 1994.
[44] S. Hosna, D.E. Janzen, Y.S. Mary, K.S. Resmi, R. Thomas, M. Rzaigui, W. Smirani, Molecular structure, spectroscopic, dielectric and thermal study, nonlinear optical properties, natural bond orbital, HOMO-LUMO and molecular docking analysis of $(C_6Cl_2O_4)$ $(C_{10}H_{14}N_2F)_2.2H_2O$, Spectrochim. Acta 204 (2018) 328–339, https://doi.org/10.1016/j.saa.2018.06.062.
[45] K. Jalaja, Y.S. Mary, C.Y. Panicker, S. Armakovic, S.J. Armakovic, B.K. Sagar, M. Girisha, H.S. Yathirajan, C. Van Alsenoy, Spectroscopic characterization of 4-[2-(5-ethylpyridin-2-yl)ethoxy]benzaldehyde oxime and investigation of its reactive properties by DFT calculations and molecular dynamics simulations, J. Mol. Struct. 1128 (2017) 245–256, https://doi.org/10.1016/j.molstruc.2016.08.075.
[46] Y.S. Mary, C.Y. Panicker, H.T. Varghese, C. Van Alsenoy, M. Prochazkova, R. Sevcik, P. Pazdera, Acid-base properties, FT-IR, FT-Raman spectroscopy and computational study of 1-(pyrid-4-yl)piperazine, Spectrochim. Acta 121 (2014) 436–444, https://doi.org/10.1016/j.saa.2013.10.119.
[47] C.Y. Panicker, H.T. Varghese, K.C. Mariamma, K. John, S. Mathew, J. Vinsova, C. Van Alsenoy, Y.S. Mary, Spectroscopic investigations and computational study of 2-[acetyl(4-Bromo phenyl)carbamoyl]-4-chlorophenyl acetate, J. Raman Spectrosc. 41 (2010) 707–716, https://doi.org/10.1002/jrs.2492.
[48] Y.S. Mary, K. Raju, C.Y. Panicker, A.A. Al-Saadi, T. Thiemann, C. Van Alsenoy, Molecular conformational analysis, vibrational spectra, NBO analysis and first hyperpolarizability of (2*E*)-3-phenylprop-2-enoic anhydride based on density functional theory calculations, Spectrochim. Acta 128 (2014) 638–646, https://doi.org/10.1016/j.saa.2014.02.194.
[49] R. Renjith, Y.S. Mary, C.Y. Panicker, H.T. Varghese, M. Pakosinska-Parys, C. Van Alsenoy, A.A. Al-Saadi, Spectroscopic (FT-IR, FT-Raman) investigations and quantum chemical calculations of 1,7,8,9-tetrachloro-10,10-dimethoxy-4-{3-[4-(3-methoxyphenyl)piperazin-1-yl]propyl}-4-azatricyclo[5.2.1.$0^{2,6}$]dec-8-ene-3,5-dione, Spectrochim, Acta 129 (2014) 438–450, https://doi.org/10.1016/j.saa.2014.03.077.
[50] G. Socrates, Infrared characteristic group frequencies, John Wiley and Sons, New York, 1980.
[51] K. Fulki, Role of frontier orbitals in chemical reactions, Science 218 (4574) (1982) 747–754, https://doi.org/10.1126/science.218.4574.747.
[52] J. Aihara, Reduced HOMO-LUMO gap as an index of kinetic stability for polycyclic aromatic hydrocarbons, J. Phys. Chem. A 103 (1999) 7487–7495, https://doi.org/10.1021/jp9900092i.
[53] A. Pirnau, V. Chis, O. Oniga, N. Leopold, L. Szabo, M. Baias, O. Cozar, Vibrational and DFT study of 5-(3-pyridyl-methylidene)-thiazolidine-2-thione-4-one, Vib. Spectrosc. 48 (2008) 289–296, https://doi.org/10.1016/j.vibspec.2008.01.012.
[54] Y. Ruiz-Morales, HOMO–LUMO gap as an index of molecular size and structure for polycyclic aromatic hydrocarbons (PAHs) and asphaltenes: a theoretical study, J. Phys. Chem. A 106 (2002) 11283–11308, https://doi.org/10.1021/jp021152e.
[55] K. Haruna, V.S. Kumar, Y. Sheena Mary, S.A. Popoola, R. Thomas, M.S. Roxy, A.A. Al-Saadi, Conformational profile, vibrational assignments, NLO properties and molecular docking of biologically active herbicide 1,1-dimethyl-3-phenylurea, Heliyon 5 (6) (2019) e01987.
[56] G.D.R. Matos, D.Y. Kyu, H.H. Loeffler, J.D. Chodera, M.R. Shirts, D.L. Mobley, Approaches for calculating solvation free energies and enthalpies demonstrated with an update of the FreeSolv database, J. Chem. Eng. Data 62 (2017) 1559–1569, https://doi.org/10.1021/acs.jced.7b00104.
[57] R.F. Ribeiro, A.V. Marenich, C.J. Cramer, D.G. Truhlar, Prediction of SAMPL2 aqueous solvation free energies and tautomeric ratios using the SM8, SM8AD, and SMD solvation models, J. Comput. Aided Mol. Des. 24 (2010) 317–333, https://doi.org/10.1007/s10822-010-9333-9.
[58] P. Politzer, P.R. Laurence, K. Jayasuriya, Molecular electrostatic potentials: an effective tool for the elucidation of biochemical phenomena, Environ. Health Perspect. 61 (1985) 191–202, https://doi.org/10.1289/ehp.8561191.

[59] J. Lu, W.R. Kobertz, C. Deutsch, Mapping the electrostatic potential within the ribosomal exit tunnel, J. Mol. Biol. 371 (2007) 1378–1391, https://doi.org/10.1016/j.jmb.2007.06.038.
[60] T. Karthick, P. Tandon, Computational approaches to find the active binding sites of biological targets against busulfan, J. Mol. Model. 22 (2016) 142, https://doi.org/10.1007/s00894-016-3015-z.
[61] K.B. Benzon, Y.S. Mary, H.T. Varghese, C.Y. Panicker, S. Armakovic, S.J. Armakovic, K. Pradhan, A.K. Nanda, C. Van Alsenoy, Spectroscopic, DFT, molecular dynamics and molecular docking study of 1-butyl-2-(4-hydroxyphenyl)-4,5-dimethyl-imidazole-3-oxide, J. Mol. Struct. 1134 (2017) 330–344, https://doi.org/10.1016/j.molstruc.2016.12.100.
[62] E.D. Glendening, A.E. Reed, J.E. Carpenter, F. Weinhold, NBO version 3.1, TCI, University of Wisconsin, Madison, 1998.
[63] A.E. Reed, L.A. Curtiss, F. Weinhold, Intermolecular interactions from a natural bond orbital, donor-acceptor, view point, Chem. Rev. 88 (1988) 899–926, https://doi.org/10.1021/cr00088a005.
[64] A.D. Becke, K.E. Edgecombe, A simple measure of electron localization in atomic and molecular systems, J. Chem. Phys. 92 (1990) 5397–5403, https://doi.org/10.1063/1.458517.
[65] B. Silvi, A. Savin, Classification of chemical bonds based on topological analysis of electron localization functions, Nature 371 (1994) 683–686. https://www.nature.com/articles/371683a0.
[66] J.S. Al-Otaibi, Y.S. Mary, Y.S. Mary, S. Soman, N. Acharjee, B. Narayana, Theoreticl and experimental investigation of a pyrazole derivative-solvation effects, reactivity analysis and MD simulations, Chem. Phys. Lett. 793 (2022), https://doi.org/10.1016/j.cplett.2022.139469 139469.
[67] R.F.W. Bader, In Atoms in Molecules: A quantum theory, Clarendon Press, Oxford, 1990.
[68] R.F.W. Bader, H. Essen, The characterization of atomic interactions, J. Chem. Phys. 80 (1984) 1943–1960, https://doi.org/10.1063/1.446956.
[69] J.C. Garcia, E.R. Johnson, S. Kleinan, R. Chaudret, J.P. Piquemal, D.N. Beratan, W. Yang, NCIPLOT: a program for plotting non-covalent interaction regions, J. Chem. Theory Comput. 7 (2011) 625–632, https://doi.org/10.1021/ct100641a.
[70] V.S. Kumar, Y.S. Mary, Y.S. Mary, G. Serdaroglu, A.S. Rad, M.S. Roxy, P.S. Majula, B.K. Sarojini, Conformational analysis and DFT investigations of two triazole derivatives and its halogenated substitution by using spectroscopy, AIM and Molecular docking, Chemical Data Collections 31 (2021), https://doi.org/10.1016/j.cdc.2020.100625 100625.
[71] A.C. Melvin, T.A. Annabelle, N.M. Marlon, A. Ghosh, In-silico evaluation of binding of phytochemicals from bayati (AnamirtacocculusLinn) to the gluthione-s-transferase of Asian corn borer (OstriniafurnacalisGuenee), J. Biomol. Struct. Dyn. (2022), https://doi.org/10.1080/07391102.2022.2036240.
[72] L.H. Al-Wahaibi, M. Abdalla, Y.S. Mary, Y.S. Mary, R.A. Costa, M. Rana, A.A. El-Emam, H.M. Hassan, N.H. Al-Shaalan, Spectroscopic, solvation effects and MD simulation of an adamantane-carbohyrazide derivative, a potential antiviral agent, Polycyclic Aromat. Compd. (2022), https://doi.org/10.1080/10406638.2022.2039233.
[73] J.S. Al-Otaibi, Y.S. Mary, Y.S. Mary, S. Aayisha, DFT conformational, wavefunction based reactivity analysis, docking and MD simulations of a carboxamide derivative with potential anticancer activity, Polycyclic Aromat. Compd. (2022), https://doi.org/10.1080/10406638.2022.2032765.
[74] J.S. Al-Otaibi, Y.S. Mary, Y.S. Mary, R. Yadav, Structural and reactivity studies of pravadoline – An ionic liquid, with reference to its wavefunction-relative properties using DFT and MD simulations, J. Mol. Struct. 1245 (2021), https://doi.org/10.1016/j.molstruc.2021.131074 131074.
[75] G. Venkatesh, Y. Sixto-Lopez, P. Vennila, Y.S. Mary, J. Correa-Basurto, Y.S. Mary, A. Manikandan, An investigation on the molecular structure, interaction with metal clusters, anti-covid-19 ability of 2-deoxy-D-glucose: DFT calculations, MD and docking simulations, J. Mol. Struct. 1258 (2022), https://doi.org/10.1016/j.molstruc.2022.132678 132678.